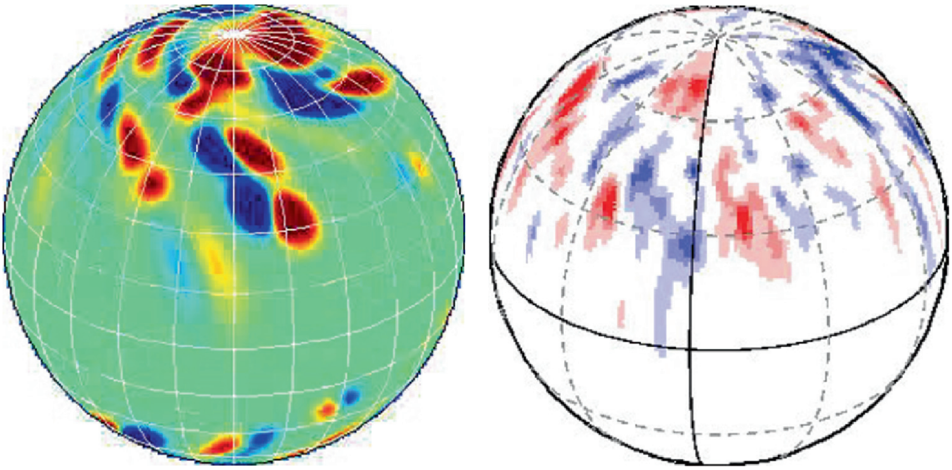

Plate 1 (Fig. 2.16). (Left) Radial magnetic field simulated with a surface flux transport model assuming solar-like transport parameters, but for a flux emergence rate that is 30× solar, and a larger latitudinal range for flux emergence, combined with a meridional flow peaking at 100 m/s (∼5× solar). (Right) Observed radial magnetic field distribution for the rapidly rotating star AB Doradus ($P_{\rm rot} = 0.51$ d). (From Holzwarth *et al.*, 2007. Reproduced with permission © Wiley-VCH Verlag GmbH & Co. KGaA.)

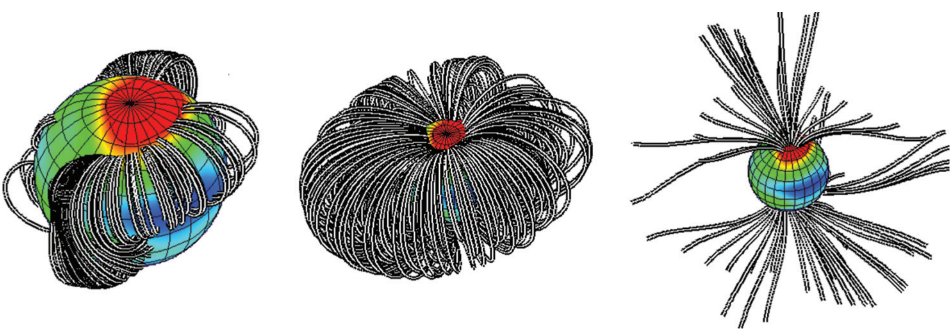

Plate 2 (Fig. 3.9). Inferred magnetic field structure of the classical T Tauri star BP Tau. Surface shading shows photospheric magnetic field strength; the three figures from left to right show estimated near-field closed, far-field closed, and open magnetic field lines. Red and blue tones indicate oppositely directed radial magnetic field strengths. (From Gregory *et al.,* 2008.)

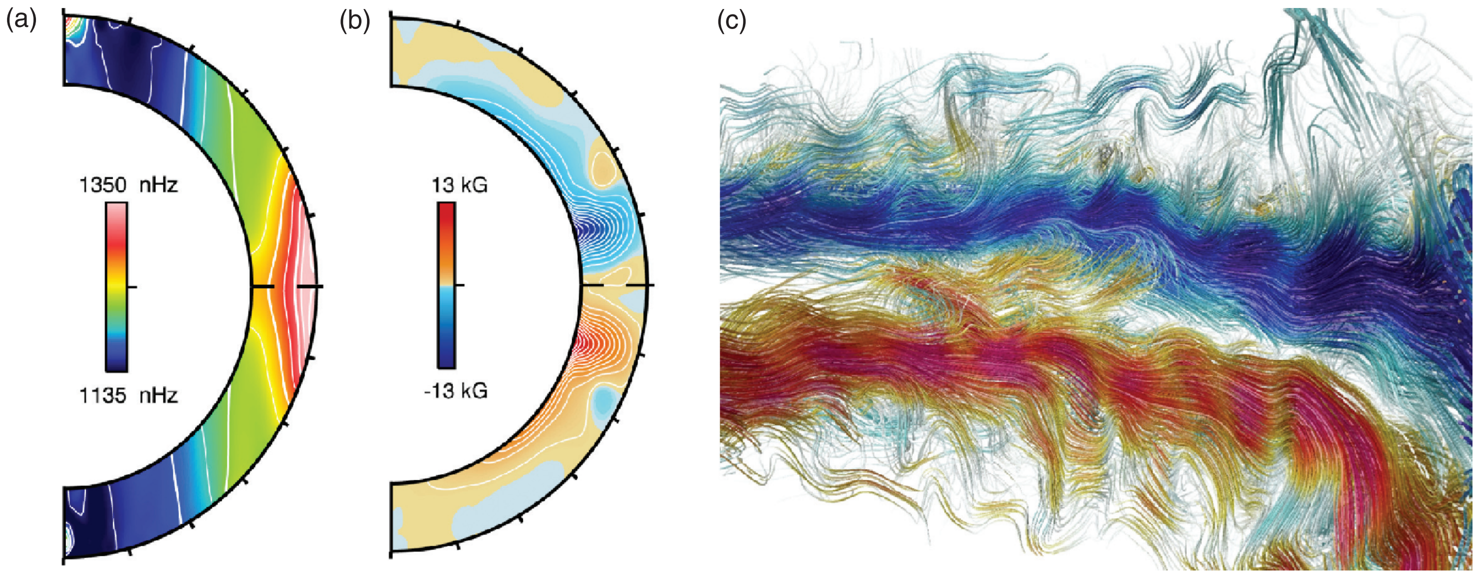

Plate 3 (Fig. 5.4). Rotational shear and toroidal fields in a global 3D dynamo simulation of a solar-type star rotating at three times the solar rate. (a) Angular velocity Ω and (b) toroidal field $\langle B_\phi \rangle$, averaged over longitude and time. (c) A 3D rendering of magnetic field lines in a portion of the convection zone, spanning about 50° in longitude. Red and blue lines denote positive and negative B_ϕ respectively. The view is radially outward from a vantage point under the convection zone and slightly above (north of) the equator. (From Brown *et al.,* 2009.)

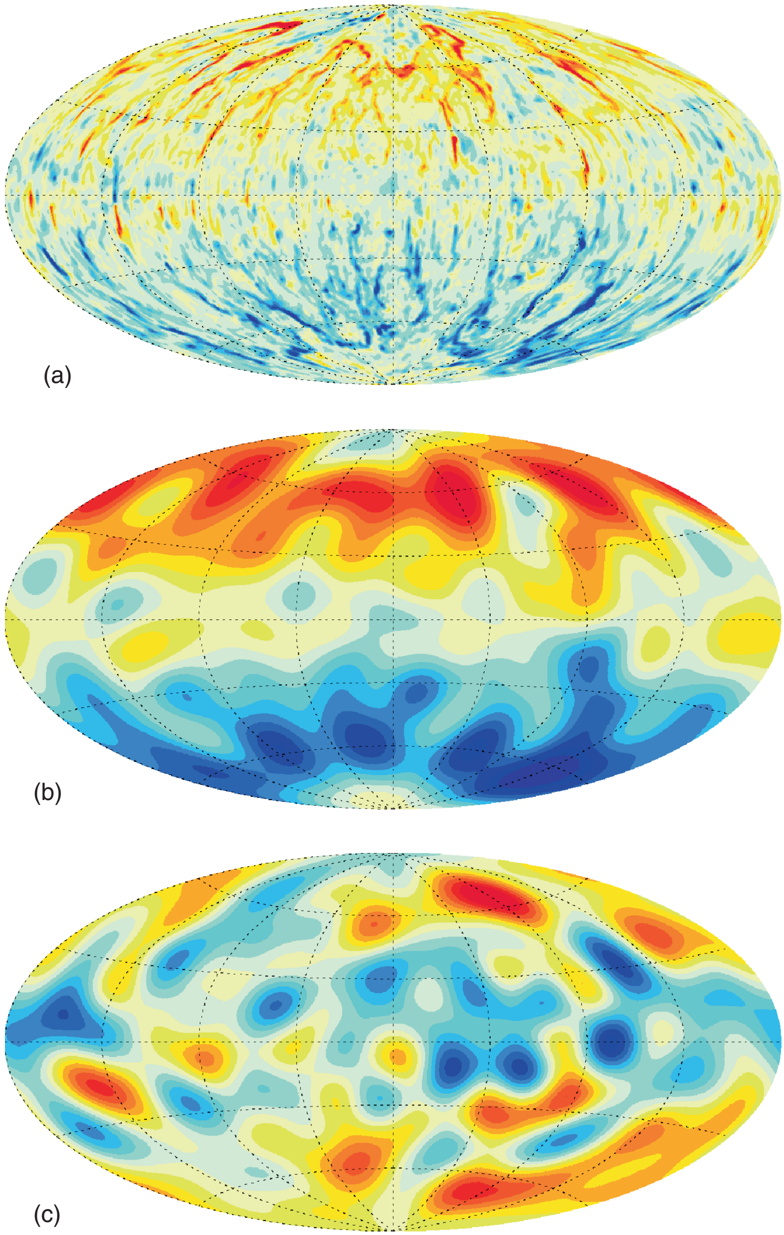

Plate 4 (Fig. 7.7). Snapshots of the radial magnetic field component on the outer boundary from numerical dynamo models. Red areas are used for outward flux and blue for inward flux (arbitrary contour steps in each panel). Color-scale indicates absolute amplitude. (a) Model parameters $E = 10^{-5}$, $R_a^* = 0.12$, $P_m = 0.8$, $P_r = 1$. (b) Same field low-pass filtered to harmonic degrees $n < 14$. (c) Model parameters $E = 10^{-5}$, $R_a^* = 0.17$, $P_m = 0.5$, $P_r = 1$, low-pass filtered. R_m is approximately 900 in both cases; R_{ol} is 0.125 in (a) and (b), and 0.19 in (c).

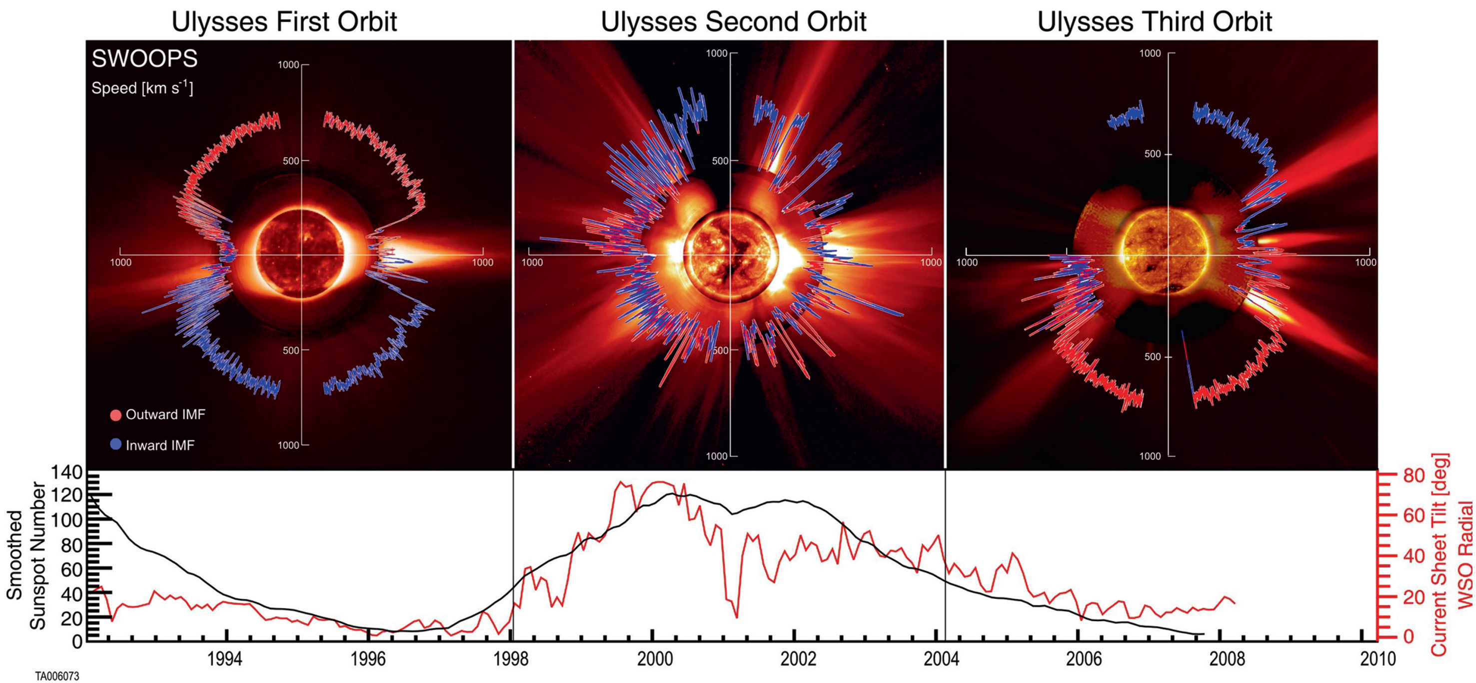

Plate 5 (Fig. 8.2). (Top) Polar plots of solar wind speed for almost three complete Ulysses polar orbits about the Sun plotted over solar images characteristic of sunspot minimum (8/17/1996), maximum (12/07/2000), and again minimum (03/28/2006); inward/outward directed field is shown in blue/red. In each panel the earliest times are near aphelion at the nine o'clock positions, with time progressing counterclockwise. The nested solar images are from SOHO's EIT (Fe XII at 19.5 nm), the Mauna Loa K-coronameter (700–950 nm), and the SOHO LASCO/C2 white-light coronagraph. (Bottom) Contemporaneous smoothed sunspot number (black) and tilt of the heliospheric current sheet (red). (From McComas *et al.*, 2008.)

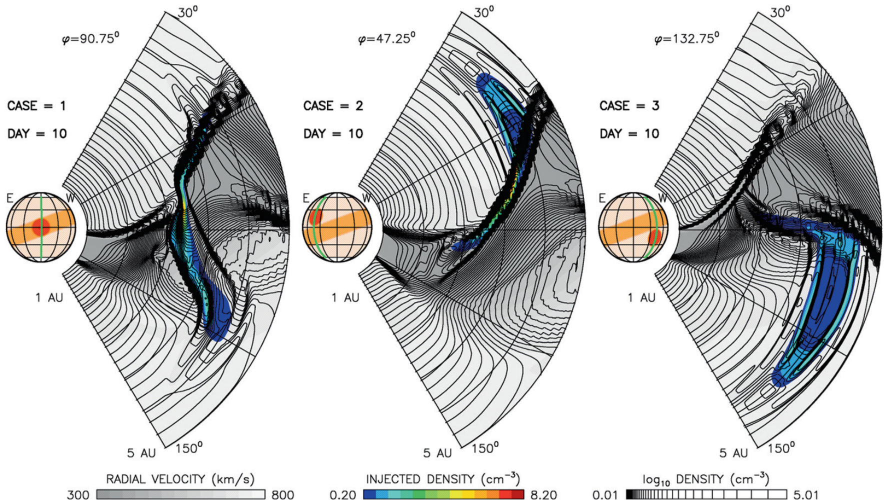

Plate 6 (Fig. 8.12). Meridional plane cross sections of 3D gas-dynamic ICME simulations viewed 10 days after launch at the inner boundary, initially moving at the speed of the fast wind. Radial velocity is shown as grey scale, ICME density in color, and the ambient wind density by contours. Left: ICME injected at the equator within the band of slow wind with density and temperature 2x and 4x, respectively, that of the slow wind. Center and right: ICMEs injected to the east or west of the slow wind band, respectively, with density 8x that of the background fast flow. (From Odstrčil and Pizzo, 1999.)

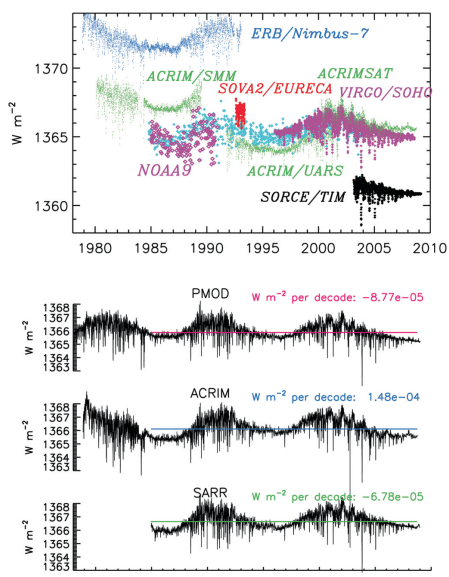

Plate 7 (Fig. 10.6). Total solar irradiance since 1978. The top panel compares these on their "native" calibration scales, above three different composite records constructed with different calibration assumptions (PMOD: C. Fröhlich; ACRIM: R. C. Willson; SARR: S. Dewitte); the slopes of these time series are shown.

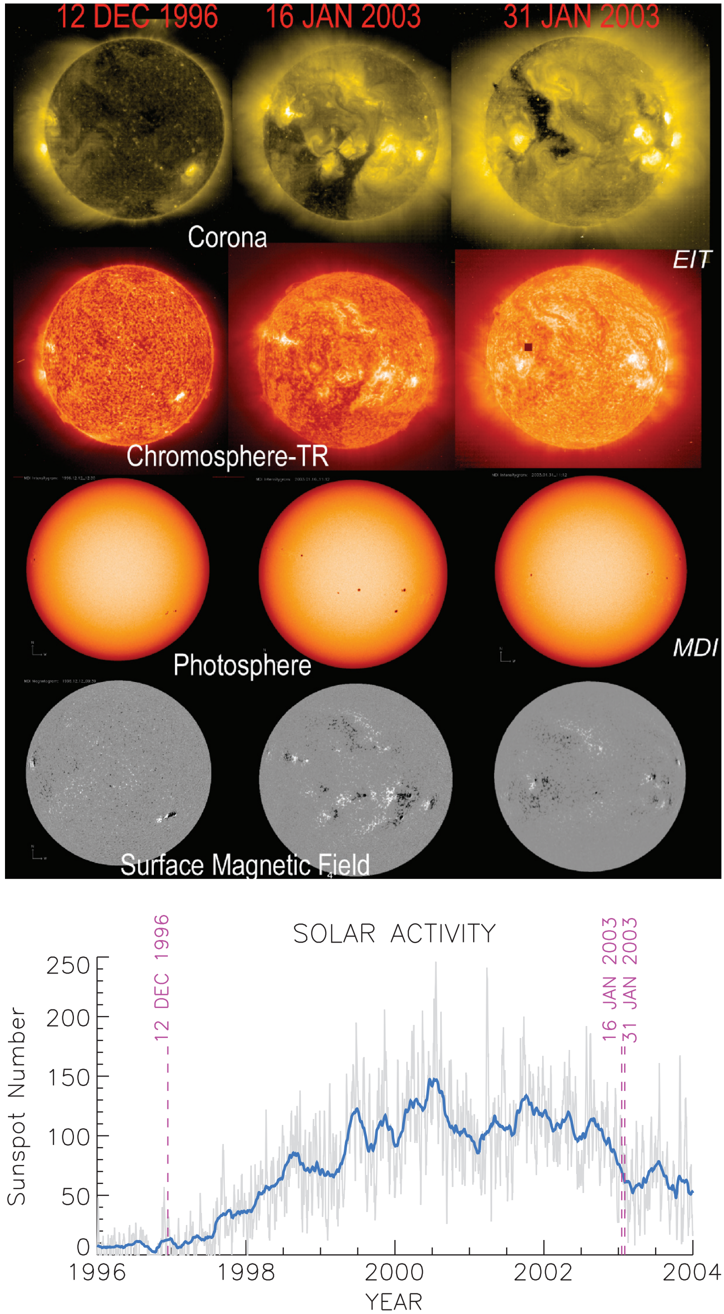

Plate 8 (Fig. 10.2). Images of the Sun's surface: magnetic map (bottom row), visible light (second row up), chromosphere/transition region (third row up), and corona (top row). The left column (December 1996) is typical of quiet cycle minima, and the two righthand columns of higher-activity states (January 2003) at different rotation phases. The bottom plot shows the sunspot number.

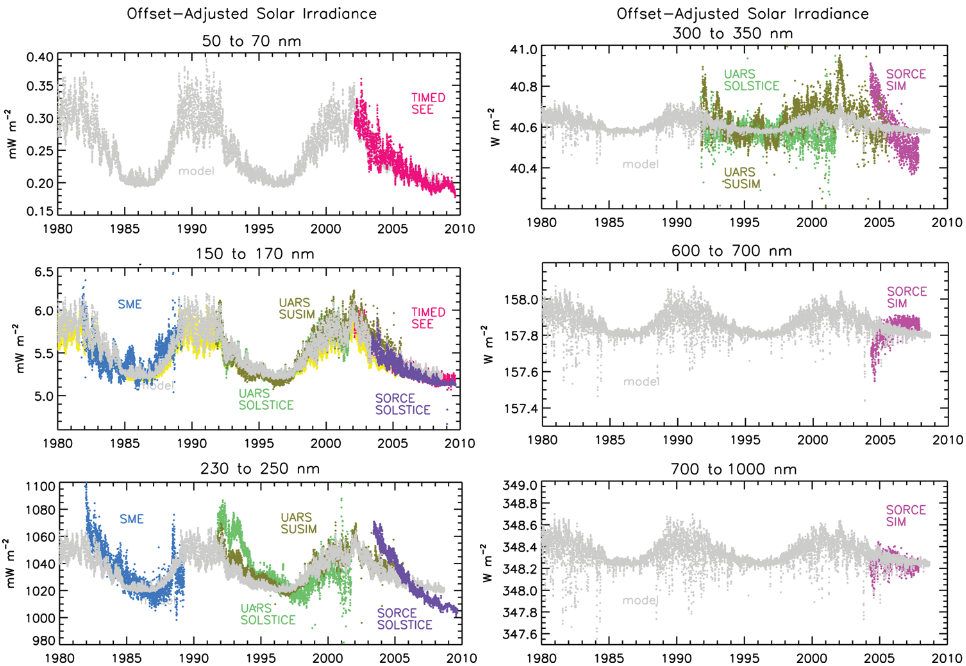

Plate 9 (Fig. 10.8). Assorted space-based observations made of the solar spectral irradiance during the past three solar cycles are compared in selected wavelength bands. From top left to bottom right: EUV (50–70 nm), FUV (150–170 nm), MUV (230–250 nm), NUV (300–350 nm), visible (600–700 nm), and IR (700–1000 nm); the curves shown have offset-adjustments to account for their different absolute calibration scales. Also shown, as the grey time series, are models of the irradiance variations in the same wavelength bands, derived by scaling the observed rotational modulation variations to the Mg (and $F_{10.7}$ for the EUV band) proxy indicators. Note the lack of daily measurements shortward of 110 nm until TIMED SEE observations commenced in 2002, and longward of 400 nm until SORCE SIM observations commenced in 2003.

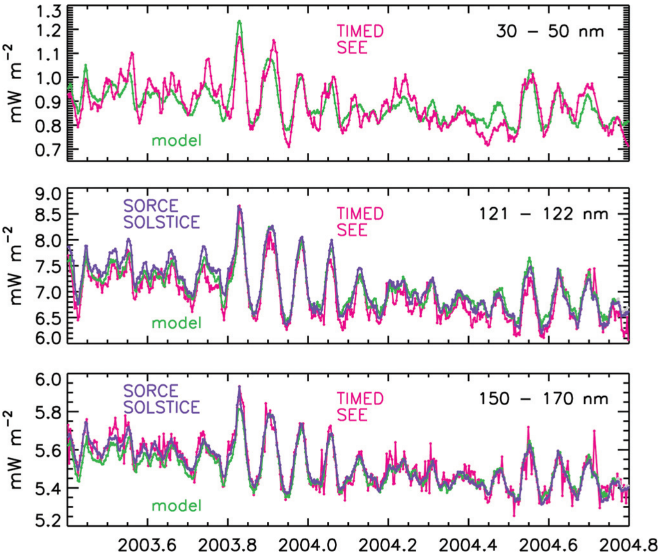

Plate 10 (Fig. 10.12). Comparison of SORCE/SOLSTICE and TIMED/SEE observations and empirical variability model estimates of irradiance in selected wavelength bands including EUV (30 to 50 nm), the Lyman α line (121–122 nm), and the far-UV (150–179 nm) wavelength bands. The comparisons indicate the good agreement among the irradiance measurements and models on the short time scales of the 27-day rotational modulation.

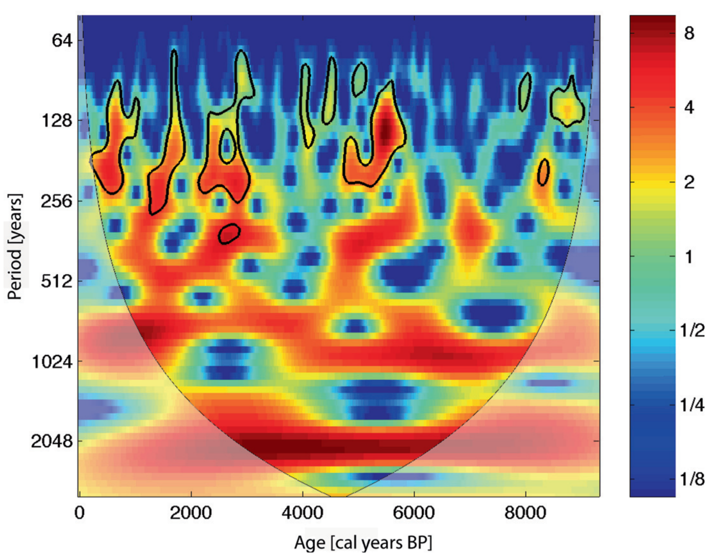

Plate 11 (Fig. 11.17). Wavelet analysis (Grinsted, 2002–4) of the solar modulation function Φ from Fig. 11.16. The color scale is a measure of the spectral power relative to the spectral power of white noise, thus measuring signal significance.

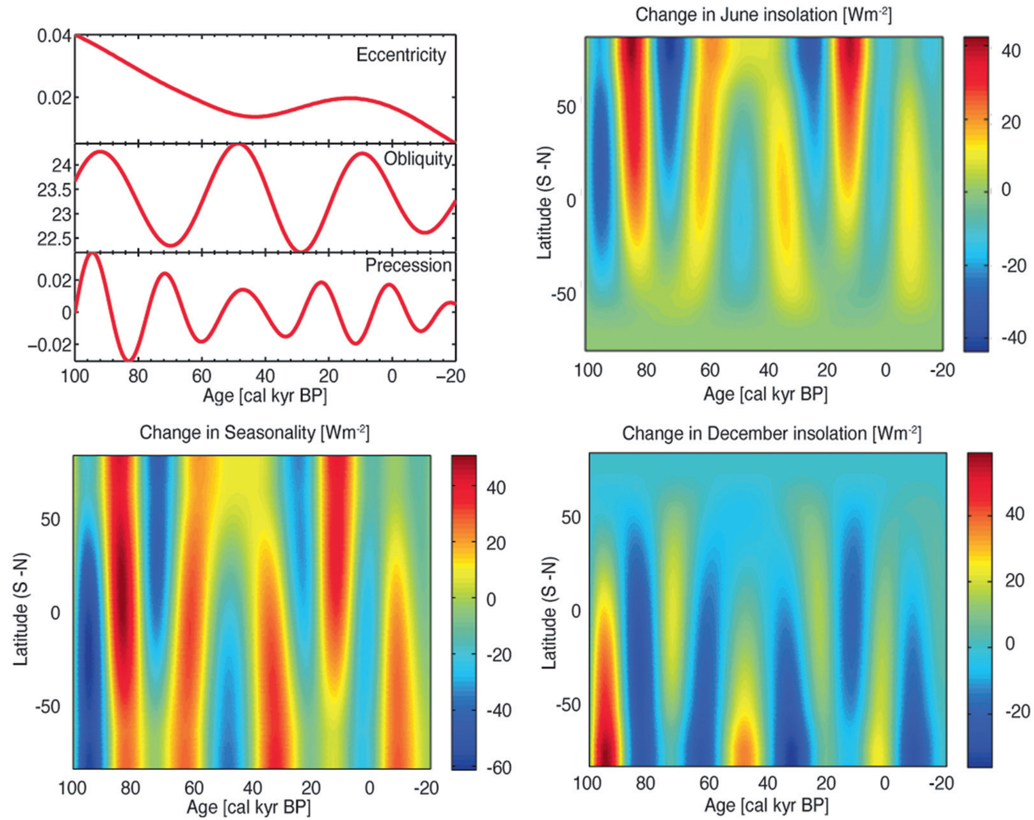

Plate 12 (Fig. 11.8). Changes in the orbital parameters of Earth and their effect on the summer (June), the winter (December) and the seasonal (June–December) insolation for the past 100 kyr and the future 20 kyr (−20 kyr BP). Shown are the deviations in $W\,m^{-2}$ from the mean values. Note the large changes at high latitudes.

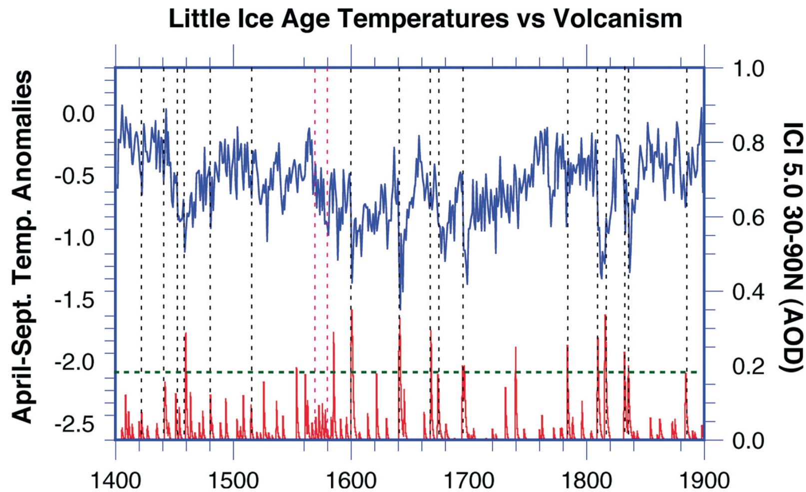

Plate 13 (Fig. 12.5). Tree-ring-based reconstruction of Northern Hemisphere (land) summer half-year temperatures (blue curve, left-hand axis) with an index of volcanism (red) for 30°–90° N in units of AOD (aerosol optical depth). The green line shows the AOD for the 1883 CE Krakatau eruption. Seventeen volcanic eruptions coincident with cooling events are marked by dashed black lines; a cluster of small eruptions is contained between the magenta lines in the late 1500s.

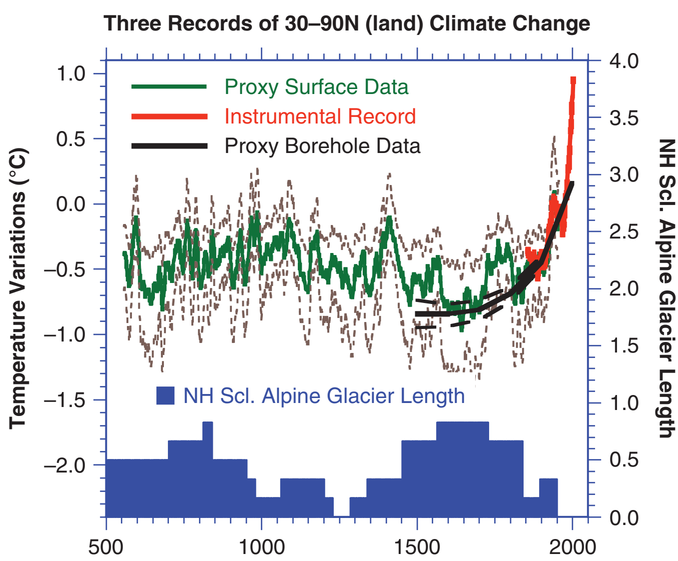

Plate 14 (Fig. 12.6). Scaled Northern-Hemisphere alpine glacier extent (Section 12.4) compared with two distinct estimates of mean annual temperature changes over land for 30°–90° N: one based on surface proxy data (tree rings, ice cores, etc., from Hegerl *et al.*, 2007), and a "borehole estimate" (based on geothermal measurements of heat flux in boreholes, from Porter and Smerdon, 2004). Figure adapted from results in Hegerl *et al.* (2007), updated through 2008, shown up to 2003 with a 10-year smoothing.

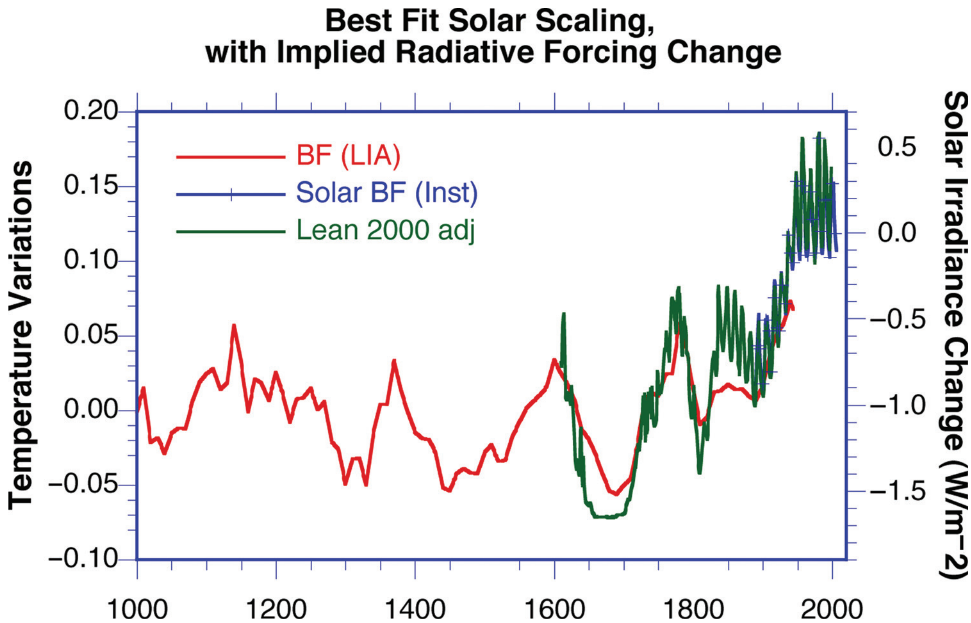

Plate 15 (Fig. 12.12). Comparison of independent estimates of solar component for the instrumental interval and Little Ice Age. The right-hand scale indicates the estimated change in total solar irradiance for the background component of the re-scaled Lean (2000) record. See Section 12.5 for a discussion of the method.

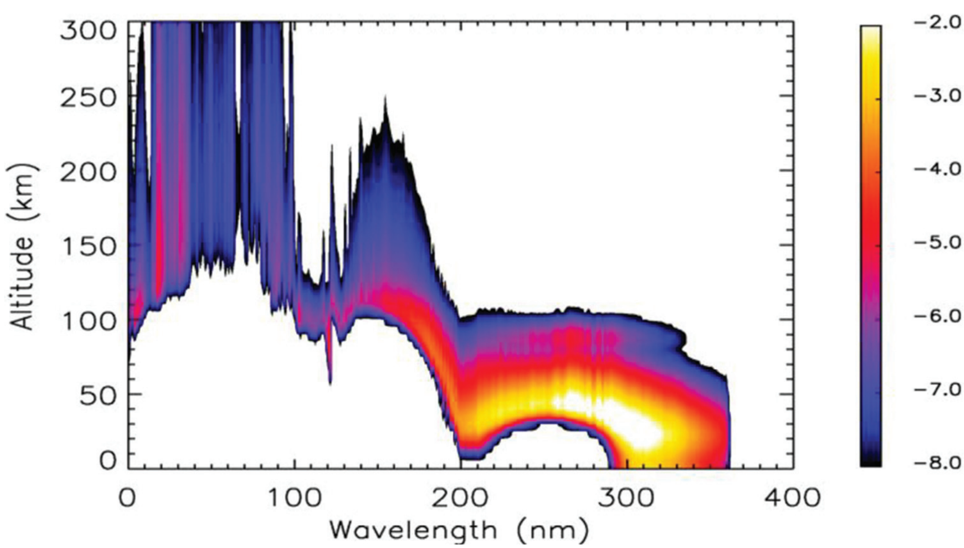

Plate 16 (Fig. 13.3). Altitude of penetration of the solar radiation as a function of wavelength. The color range shows the amount of energy deposited in the different layers of the atmosphere for the different parts of the solar spectrum (on a logarithmic scale, in units of mW m^{-3} nm^{-1}).

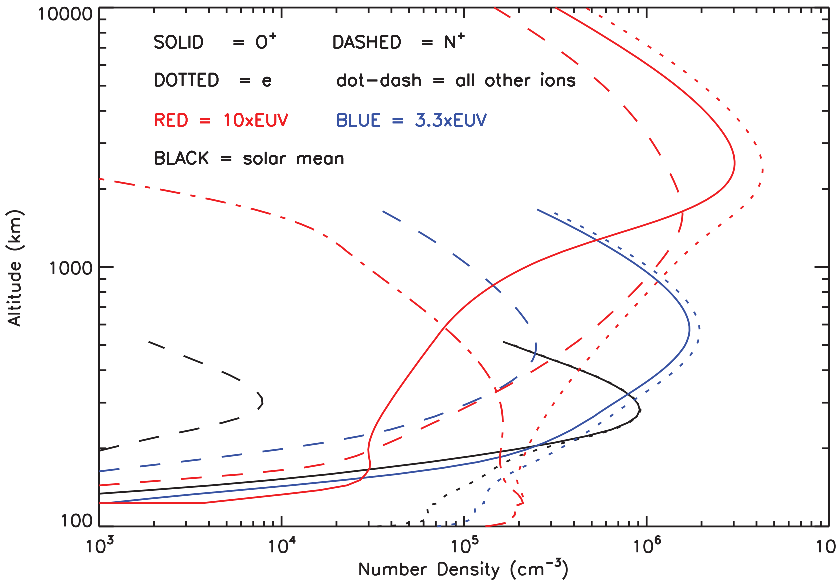

Plate 17 (Fig. 14.9). Density profiles of O^+ (solid curves), N^+ (dashed curves), and electrons (dotted curves) under different solar EUV conditions. The total density curves of all ions other than O^+ and N^+ in the 10× present EUV case is presented with the dot-dashed curve. (From Tian *et al.,* 2008b.)

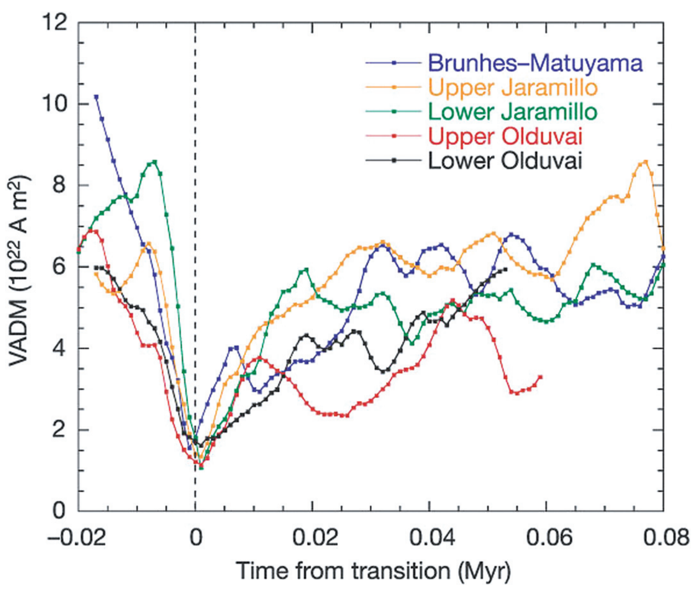

Plate 18 (Fig. 14.11). Variations in the virtual axial dipole moment across the five reversals occurring during the past 2 Myr. These are superimposed about their respective reversal epoch (with time running from right to left). A 60–80 kyr long decrease precedes each reversal. (From Valet *et al.,* 2005.)

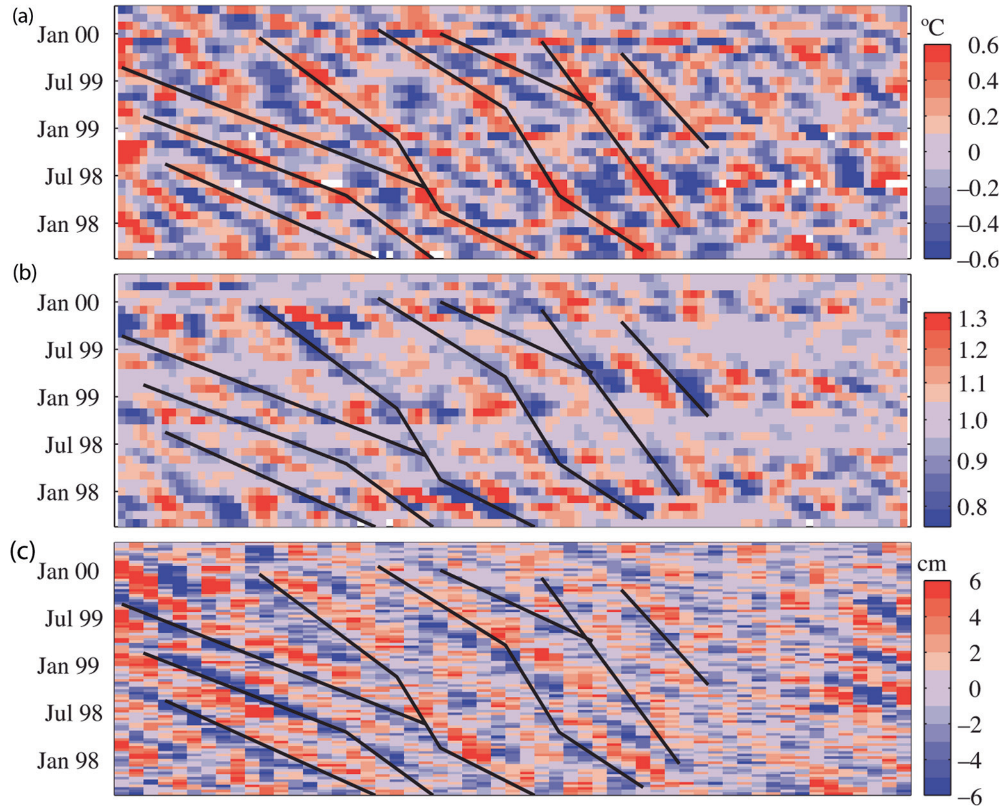

Plate 19 (Fig. 15.8). A time–longitude representation of group (energy) propagation for Rossby waves in the ocean (Hovmöller diagram), showing the variation of (a) sea surface temperature anomalies, (b) chlorophyll concentration anomalies, and (c) sea surface height anomalies. The tilt of features in this diagram reflects the westward propagation of wave groups. (From Quartly *et al*., 2003.)

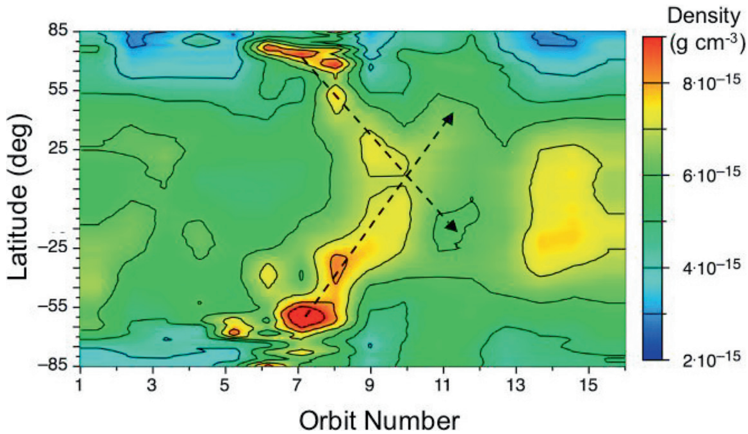

Plate 20 (Fig. 15.21). An example of a traveling atmospheric disturbance seen in density near 400 km measured by the accelerometer on the CHAMP satellite in connection with a geomagnetic disturbance. The disturbances appear to penetrate into opposite hemispheres from their origins in the Northern and Southern Hemisphere auroral zones. The simultaneous appearance in both hemispheres is due to conjugate activity. (From Forbes, 2007.)

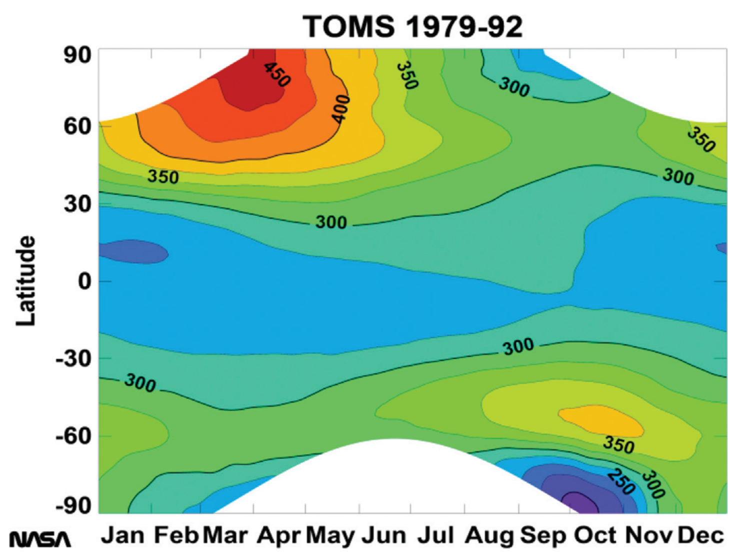

Plate 21 (Fig. 16.4). Vertically integrated ozone concentration (expressed in Dobson units or DU; at 1 DU the column depth of ozone only would equal 10 μm at sea-level pressure and average temperature) represented as a function of latitude and month of the year. The distribution is established on the basis of observations made by the spaceborne TOMS instrument between 1972 and 1992. High values at the end of the winter are visible in the Arctic (March and April) and around 60°S in September and October. The presence of the Antarctic ozone hole is visible in the Antarctic in September–November. The value of 300 DU corresponds to an ozone layer of 3 mm under STP conditions. (From NASA.)

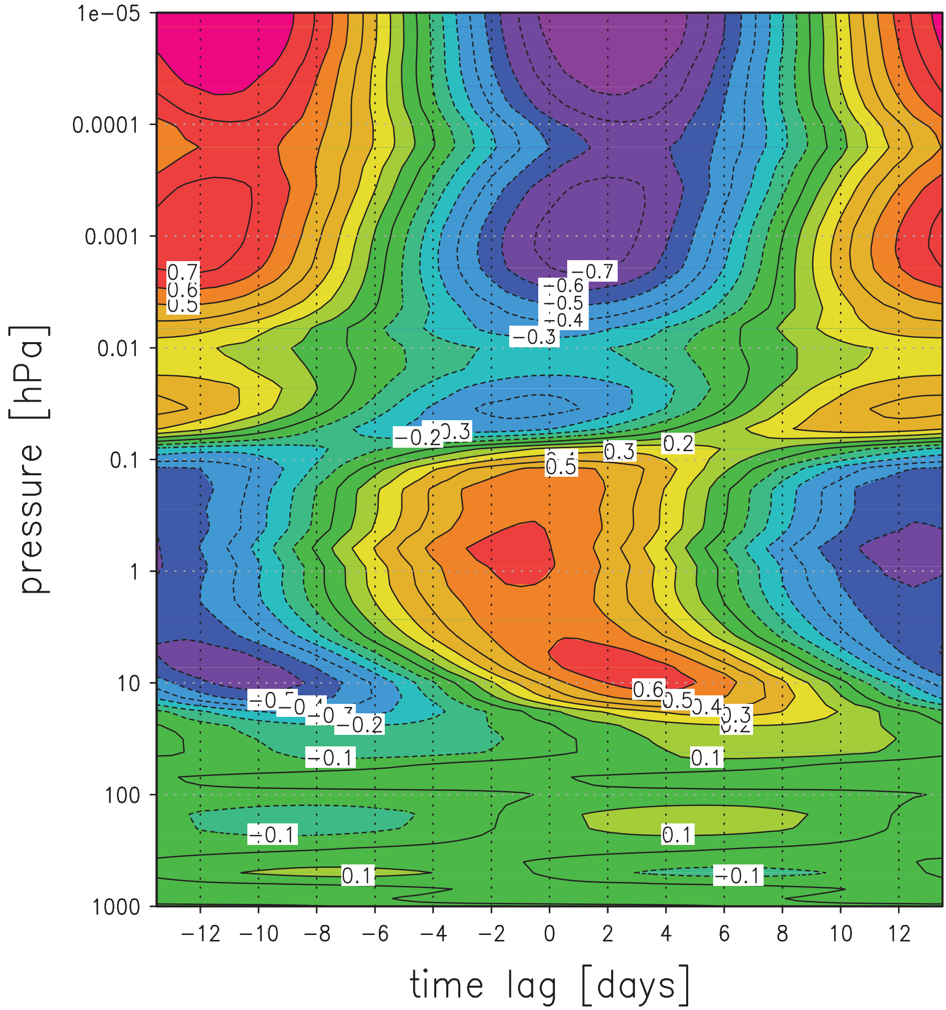

Plate 22 (Fig. 16.10). Correlation coefficient between the ozone concentration and the 27-day solar variation as a function of atmospheric pressure (hPa) for different time lags (days) as calculated by the HAMMONIA model. One notes that, at 1 hPa (about 50 km altitude) for example, the highest correlation is found when ozone and solar radiation are in phase. At 10 hPa (about 30 km), the ozone signal with a 4-day phase lag is best correlated with the 27-day solar signal. Above 0.1 hP (∼65 km), the ozone signal appears to be out of phase with the solar periodic variation. (From Gruzdev *et al.,* 2009.)

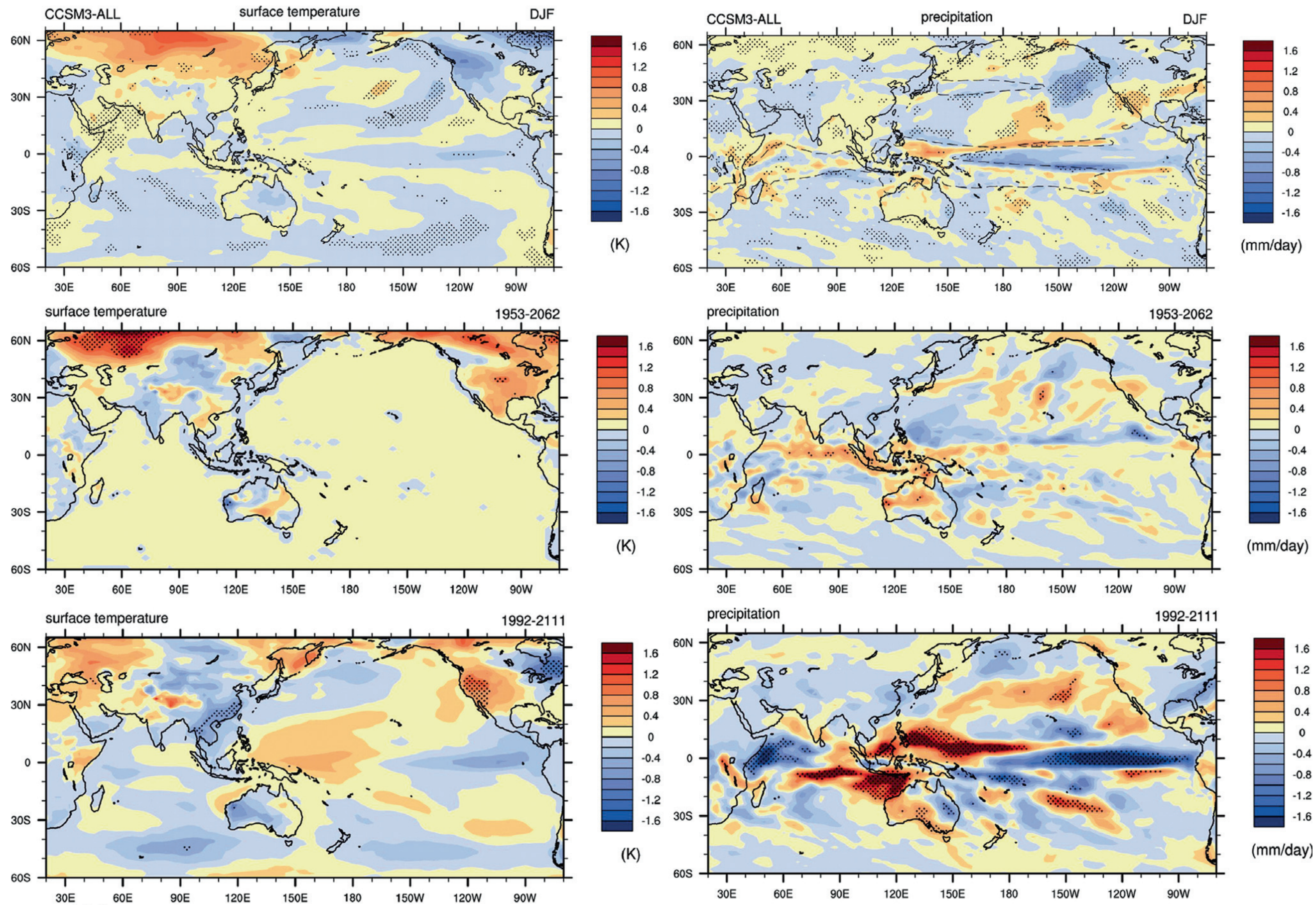

Plate 23 (Fig. 16.14). Composites (left temperature; right precipitation) for simulated peaks in the 11-year solar cycle. Bottom-up coupled air-sea mechanism (top panels) and top-down stratospheric ozone mechanism (middle panels) are additive to strengthen convection in the tropical Pacific and produce a stronger La Niña-like response to peaks in solar forcing (bottom panels). (From Meehl *et al.,* 2009.)